Assessment of x-ray Scatter for the Micro-CT Subsystem of the FLEX Triumph™ Preclinical PET-CT Scanner

Daniel Gutierrez, *Member, IEEE*, and Habib Zaidi, *Senior Member, IEEE*

***Abstract*–This work aims at assessing x-ray scatter and more specifically the scatter to primary ratio (SPR) for the micro-CT subsystem of the FLEX Triumph™ preclinical PET-CT scanner. Two approaches were used: the experimental single blocker method and Monte Carlo (MC) simulations using the MCNP4C code. For the experimental setup, five cylindrical blockers with diameters ranging between 3.0 and 11.65 mm were used to assess the SPR using a polyethylene phantom (d=50mm). The beams energy influence was studied by scanning the phantom at 30, 50 and 80 kV (mag=1.3). Likewise, additional acquisitions at 50 kV were performed with a magnification of 2.0 to evaluate the impact of geometrical magnification and using a Plexiglas phantom (d=25mm) filled with water at 50 kV (mag=1.3) to assess the influence of the size and composition of the phantom. For each condition, the five blocker SPR results were linearly interpolated to obtain the SPR without the blocker. Central and peripheral SPR values were obtained by rotating the source and detector and were fitted with a Gaussian function. MC simulations were carried out using the MCNP4C code where the estimates were also fitted with a Gaussian function. The comparison showed that MC simulations can reproduce well the experimental results, at least in the region inside the phantom. The highest difference was obtained with the small phantom in the peripheral regions. The maximum SPR (0.562) was obtained at 30kV and magnification of 1.3 using the large phantom. The full SPR profile was calculated using MC simulations and used to express its dependency on beam energy and phantom diameter (quadratic), and air gap (asymptotic). The obtained results are in good agreement with theoretical predictions. MC is a very good alternative to experimental measurements of x-ray scatter in micro-CT imaging and can be used to validate novel scatter correction techniques. This will also improve the accuracy of CTAC on preclinical PET-CT systems.**

***Index Terms*— Computed Tomography (CT), micro-CT, x-ray scatter, PET-CT, Monte Carlo.**

I. INTRODUCTION

Small-animal imaging has become an essential tool to study molecular pathways of disease and to test therapeutic approaches of human disease. Preclinical PET-CT units are well established research instruments in molecular imaging and the FLEX Triumph™ system is a commercial systems offering the capability of tri-modality imaging including PET, SPECT, and CT subsystems [1], but available in our facility as a dual-modality PET-CT system. However, most pre-clinical PET image quantification suffers from many physical degrading factors, one of them being photon attenuation which can be corrected for using different techniques [2]. The common technique implemented on combined PET-CT systems is CT-based attenuation correction (CTAC), which must be performed using CT images of the highest possible quality [3, 4].

Most micro-CT units uses a cone-beam flat panel detector [5] that suffers from scatter effects thus substantially reducing the quality of CT images [6, 7]. To assess the impact of x-ray scatter on the accuracy of CTAC [8], one must characterize the scatter to primary ratio (SPR) of these micro-CT systems. The determination of SPR for these devices has been addressed using various experimental approaches and through computer simulations. One of the most comprehensive studies related to scatter estimation on flat panel detectors was carried out by Boone et al.[9] where four different experimental methods were assessed. These include edge spread of the point spread function (PSF) of scatter, beam-stop, scatter medium reposition and slat method. And compared them to Monte Carlo simulations in an experimental mammography device.

The scatter magnitude and its impact when realizing CT acquisitions from body parts with sizes going from extremities up to body sizes was explored in an elegant study by Siewerdsen and Jaffray [7] where the measurement method used a beam-stop setup with a rotating phantom placed inside a fixed PMMA device of variable size to mimic different body sizes.

On other studies focused on flat panel micro-CT devices, often used for breast imaging, the SPR measurements were performed using the beam-stop array method [10, 11], the slat method [12] and the beam-stop and aperture methods combined with Monte Carlo simulations [13]. Most of these studies, were realized with a static imaging device, while the tomographic acquisition was obtained by rotating the object.

The SPR evaluation and its impact on image quality for cone-beam micro-CT devices was evaluated using the single blocker method by Ni et al.[14] where the size of the beam was modulated using slit collimators to obtain a fan-beam geometry reproducing a method already used by Chow et al.[15]. More recent contributions described various methods of scatter estimation and correction for flat panel CT devices in radiation therapy applications [16, 17] where the scatter is

This work was supported by the Swiss National Foundation under grant No. 31003A-125246.

Daniel Gutierrez is with Division of Nuclear Medicine, Geneva University Hospital, CH-1211 Geneva, Switzerland
(e-mail: Daniel.GutierrezRios@unige.ch)
Habib Zaidi is with the Division of Nuclear Medicine, Geneva University Hospital, CH-1211 Geneva, Switzerland and Geneva Neuroscience Center, Geneva University, Geneva, Switzerland
(e-mail: habib.zaidi@hcuge.ch).

estimated from the acquisition of a limited number of projections made with an array blocker.

Monte Carlo methods are often proposed as an alternative to demanding experimental measurements to evaluate the SPR for different systems owing to their flexibility and unlimited possibilities offered in terms of quantification of physical parameters that are difficult or even impossible to determine by experimental measurements [18-24]. However, this method is time consuming and suffers from difficulties associated with the creation of precise numerical models for complex situations. Actually it is possible to run individualized Monte Carlo calculations in a reasonable amount of time using high powered computing workstations or distributed computing networks. Hybrid approaches (analytical calculations using Monte Carlo data) have also been considered to decrease the computation time [23, 25].

In this work we combine experimental an Monte Carlo simulations to minimise difficulties to assess the scatter to primary ratio (SPR) of the FLEX Triumph™ preclinical PET-CT scanner. Due to the vertical layout of this commercial device and the rotation of the source and the detector around the imaged object, we opted for the single blocker method (SBM) used for the first time by Yaffe et al. [26] and Johns and Yaffe [27] on a prototype fan-beam devices. This choice was motivated by the little needed intervention on the imaging device with the disadvantage of obtaining the SPR only on a small part of the detector. Monte Carlo simulations were performed using the MCNP4C code to obtain the full profile of the SPR as well as the evaluation of the influence of the acquisition parameters on this result.

II. Materials and Methods

A. Micro-CT imaging system

The data was acquired using the micro-CT subsystem of the commercial the FLEX Triumph™ preclinical PET/CT scanner (Gamma Medica-Ideas, Nortridge, CA)[1]. PET and CT subsystems are mounted on the same gantry allowing functional and anatomical imaging only with table translation.

The micro-CT subsystem is composed of an x-ray tube with an air-cooled fixed tungsten anode with a focal spot of 50 µm and an aluminium output window of 0.7 mm. The maximum tube power is 40 W with voltage ranging from 30 kV to 80 kV. The tube current at each voltage is set by a calibration procedure that consists of data acquisition without any object in the field of view at 3 levels of exposure: (i) without any exposure, (ii) with full exposure, i.e. the highest tube current which gives an image just below detector saturation, and (iii) with half the current used in the second acquisition to verify the linear response of the detector. Acquisitions are performed automatically at the maximum exposure similar to the second acquisition of the calibration procedure.

The x-ray flat panel detector is the Hamamatsu C7942, it is made of a CsI scintillator plate. This detector of 0.15 mm thickness has an active area of 12×12 cm^2 with a pixel pitch of 50 μm^2 (2400×2400 pixels). The detector is protected by a 1 mm thick aluminium cover that render it insensitive to photons having energies below 15 keV [28]. The source to detector distance is constant (*SDD*=290 mm) but the device is able to realize a geometrical magnification (*mag.=SDD/SOD*) by changing the source to object distance (*SOD*) by the displacement of the source-detector couple and leaving the object always at the center of rotation. In this way, the magnification can be set between 1.3 (*SOD*=223 mm) and 2.5 (*SOD*=116 mm).

B. Test phantoms

To evaluate the SPR we have used two test phantoms. The first one is a rat-size cylindrical polyethylene phantom with a diameter of 50 mm and a height of 250 mm. The second phantom is a mouse-size cylindrical Plexiglas phantom with a diameter of 25 mm and a height of 240 mm filled with water.

C. Single Blocker Method

The experimental measurement of SPR was done with the Single Blocker method (SBM). Five cylindrical lead blockers of 3.0, 5.1, 7.0, 9.8 and 11.65 mm diameter and with thickness of 4 mm are larger than 96 times the thickness of the HVL (0.041 mm of lead) for the highest effective beam energy (80 kV).

The SBM was first employed by Yaffe et al. [26] and we have employed the method used on the work of Johns and Yaffe [27]. In this method, a first acquisition of the phantom is performed without measurement of scatter (Fig. 1a):

$$M_1 = P + S = P' + P'' + S \tag{1}$$

where M_1 is the total flux to the detector equal to the sum of S the scatter produced by the phantom and P the primary beam passing through the phantom that is composed of P' the flux emitted by the focal spot, and P'' the off-focal spot and scattered radiation produced by the filters and collimators.

The second acquisition (M_2) is made with one of the lead blockers positioned between the x-ray tube and the phantom stopping the flux emitted by the focal spot P' (Fig. 1b):

$$M_2 = P'' + S \tag{2}$$

To determine the primary and the scatter flux, it is then necessary to estimate P''. For this purpose, Yaffe et al. [26] proposed a method that consists on the measure the total flux (M_3) without nothing on the beam path:

$$M_3 = P'_{air} + P''_{air} \tag{3}$$

where P'_{air} and P''_{air} are the focal and off-focal radiation arriving to the detector.

A forth acquisition (M_4) is then performed with nothing but the blocker in place to estimate the off-focal spot radiation P''_{air}:

$$M_4 = P''_{air} \tag{4}$$

If we calculate the SPR, we can see that experimentally it depends on the measurement of the off-focal radiation P'':

$$SPR = \frac{S}{P} = \frac{M_2 - P''}{M_1 - S} = \frac{M_2 - P''}{M_1 - \left(M_2 - P''\right)} \tag{5}$$

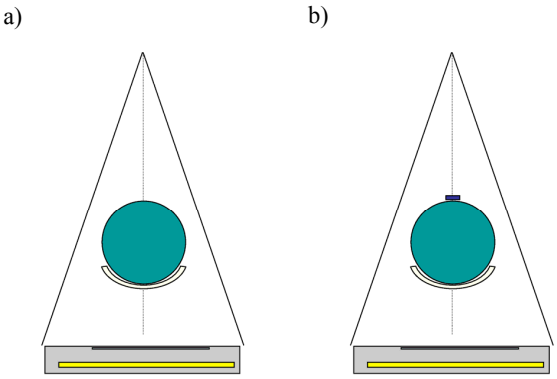

Fig. 1. Illustration of the single blocker method for scatter measurement: (a) Acquisition without blocker. (b) Acquisition with blocker.

This value can be obtained from the ratio of attenuation (*RA*) between the off-focal radiation and focal radiation:

$$RA = \frac{A''}{A'} = \frac{P''/P''_{air}}{P'/P'_{air}} \tag{6}$$

then:

$$P'' = RA \cdot A' \cdot P''_{air} \tag{7}$$

While P''_{air} can be obtained from equation (4) and the attenuation (A') of the flux emitted by the focal spot in the phantom can be easily measured:

$$A' = \frac{P'}{P'_{air}} = \frac{M_1 - M_2}{M_3 - M_4} \tag{8}$$

The problem consist on the determination. Values of *RA* between 0.81 and 0.89 were experimentally obtained by Johns and Yaffe [27] for tube potentials from 60 to 140 kV, beam filtration from 2.6 to 8 mm and water phantoms of 12 to 25 cm diameter, leading them to use a single mean value of 0.86 in their SPR measurements.

We were unable to realise this because of the limited freedom while mounting an experimental setup in this comercial PET/CT device, for this reason we have calculated the *RA* taking into account the spectrum of the beam produced by the x-ray tube ($\Phi_{kV}(E)$), to calculate the exponential attenuation produced by a phantom thickness x_{ph}:

$$A = \exp\left(-\mu\left(\Phi_{kV}(E)\right) \cdot x_{ph}\right) \tag{9}$$

We made the hypothesis that P' spectra is equal to the one of the unfiltered beam since it traverses the filters without any interaction beside photoelectric absorption of low energy photons, and that P'' spectra is roughly the spectrum of the filtered beam arriving after interacting with the filters. With these hypothesis we can calculate the ratio between A'' and A' of the spectrums $\Phi_{kV}''(E)$ and $\Phi_{kV}'(E)$ respectivelly. To simplify this calculation, we have replaced the spectrums with their respective mean energies (Table I):

$$RA = \frac{A''}{A'} = \exp\left(x_{ph} \cdot \left(\mu\left(E'_{mean}\right) - \mu\left(E''_{mean}\right)\right)\right) \tag{10}$$

Table I. Relative attenuation (*RA*) calculated using equation (10) for the two phantoms at the 6 tube voltages.

Tube Voltage (kV)	30	40	50	60	70	80
P' mean energy (keV)	21.50	25.97	30.12	33.90	37.38	40.80
P'' mean energy(keV)	22.45	27.25	31.56	35.47	39.04	42.55
Water phantom (25 mm) relative attenuation (RA)	0.90	0.87	0.96	0.96	0.96	0.98
Polyethylene phantom (50 mm) relative attenuation (RA)	0.93	0.91	0.97	0.97	0.97	0.98

We have verified the accuracy of our approximation by the calculation the *RA* for similar conditions described in the paper of Johns and Yaffe [27], and we have obtained values between 0.81 and 0.90 that are very close to the reported measured values.

With this final consideration we can calculate with the following equation:

$$SPR = \frac{S}{P} = \frac{M_2 - RA \cdot M_4 \cdot \dfrac{M_1 - M_2}{M_3 - M_4}}{M_1 - \left(M_2 - RA \cdot M_4 \cdot \dfrac{M_1 - M_2}{M_3 - M_4}\right)} \tag{11}$$

To take into the scatter reduction produced by the blocker, we interpolated to a diameter of 0 mm the SPR values obtained with the five blockers.

Finally, the device has a vertical layout (Fig. 1) and the blocker was placed directly over the phantom. For this reason, central and peripheral values of the SPR were obtained by rotating the tube-detector couple around the phantom-bed-blocker assembly and we have fitted this profile to a Gaussian function.

D. Monte Carlo simulations

The Monte Carlo N-Particle Transport Code version 4C (MCNP4C, Los Alamos National Laboratory: http://mcnp-green.lanl.gov) was used in this study. This is a general purpose code that uses nuclear and atomic data libraries for neutron energies from 10^{-11} to 20 MeV and for photon and electron energies from 10^{-3} to 1000 MeV.

This code that was originally created to simulate random processes associated with radiation interaction and detection and is often used in medical physics applications particularly in the field of diagnostic imaging.

To be able to use this code, the user must create an input text file that contains information about: geometry, materials, location and characteristics of the source, type of particles to be evaluated, type of answers desired and variance techniques to improve efficiency.

The simulation was a simplified geometry of the imaging device where only photon transport was considered. Simulation was limited to a cylindrical box corresponding to the dimensions of the device enclosure containing the following simulation elements:

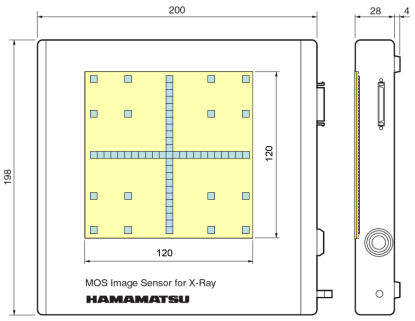

Fig. 2. Illustration of the Monte Carlo detector simulation sub-cells position (blue) related to the full detector size (yellow) over the detector schema.

- The source as a photon source with the unfiltered spectrum (https://w9.siemens.com/cms/oemproducts/Home/X-rayToolbox/spektrum/Pages/Default.aspx) corresponding to the tungsten anode
- The tube's window filter
- The phantom and the carbon fiber bed
- The detector was simulated as a multilayer of items (Fig. 2) representing the detector window, the detector sub-cells and a *SSW* (or *SSR*) card. Their order as been changed as it will be explained later.

The *Surface Source Write* (*SSW*) and card is used to write a surface source file. This file is readed in a subsequent simulation by the *Surface Source Read* (*SSR*) with the option to dissociate the particles coming from a collision from the ones that do not.

While the full gantry geometry was reproduced, the detector was only simulated on 61 sub-cells of 0.5×0.5×0.15 mm^3 size of the full physical detector (120×120×0.15 mm^3) (Fig. 2). Because of the cylindrical shape of the phantoms, the results on the remaining parts of the detector were derived using bicubic interpolation. These 61 sub-cells were set to *Pulse Height Tallies* to obtain the energy deposition in each cell per initial particle in the simulation (MeV/particle).

The compare between experimental and Monte Carlo simulation, we simulated the rotation of the tube-detector assembly and calculated the SPR for different projection angles, taking the correct sub-cell detector corresponding to the detector position (p) of the blocker in the experimental situation:

$$p = \frac{r \cdot \sin(\alpha)}{1/mag - r \cdot \cos(\alpha)/SDD} \tag{12}$$

where r is the phantom diameter, α the projection angle, *SDD* the source to detector distance (equal to 29 cm in this device) and *mag* (*mag* = *SDD*/*SOD*) the geometrical magnification.

With this rotation, we have determined the SPR profile of the central slice and fitted it to a Gaussian function for a comparison between both methods. The comparisons were realized for five different conditions: data acquisition with a magnification of 1.3 and tube potentials of 30, 50 and 80 kV with the ϕ50 mm phantom, acquisition with a magnification of 2.0 and a tube potential of 50 kV and finally acquisition of the ϕ25 mm phantom with a magnification of 1.3 and a tube potential of 50 kV.

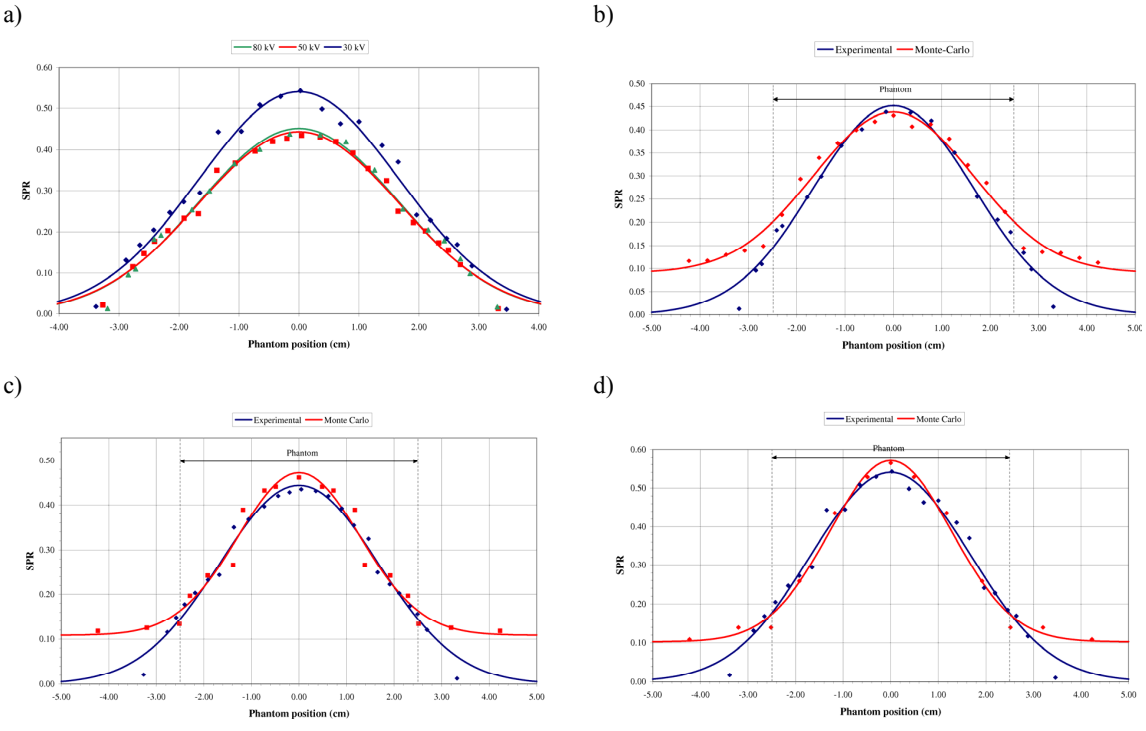

Fig. 3. SPR at different NEMA phantom positions as a function of tube potential at a magnification of 1.3. (a) Experimental results for tube potentials of 30, 50 and 80 kV. Comparison between experimental measurements and Monte Carlo simulations for: (b) 80 kV, (c) 50 kV and (d) 30 kV.

III. RESULTS

A. *Experimental and Monte Carlo simulations results*

The results of the experimental measurements of the SPR performed with the 50 mm diameter phantom at three different tube potentials are shown in Fig.3a, one can observe that the highest SPR (0.540) is obtained with a tube potential of 30 kV while the SPR for the two other tube potentials (50 and 80 kV) are quite similar (0.444 and 0.452) with a slight increase of the measured value. When comparing experimental and Monte Carlo simulation results (Fig. 3b, c and d), show that the simulation is in good agreement with the experimental results in region corresponding to the phantom where the mean relative difference between the two methods is below 2.5% for the three situations whereas the difference at the maximum SPR are between 4 and 6%.

The SPR obtained with this same phantom but with a magnification of 2.0 is shown in Fig. 4a. As expected, the SPR decreases with magnification because of the increase of the air gap and the reduction of the exposed region in the phantom. The comparison of these results with the MC simulation results shows again a good concordance (Fig. 4b) since the relative difference at the central point is below 1%. However, it increases at the peripheral part of the phantom giving a mean difference of 9.35% in the phantom region.

Finally, the influence of phantom size and chemical composition on SPR is shown in Fig. 5a for a water phantom (ϕ 2.5 cm). The SPR obtained experimentally is 0.275 at the centre of the phantom and is noticeably lower than the SPR measured (0.444) for the polyethylene phantom (ϕ 5 cm), mainly because of its smaller volume. Comparative evaluation results between experimental measurements and MC simulations (Fig. 5b), show a relatively low difference is inside the phantom region (<11.2%) and especially at its centre (<5%).

Table II. Relative difference between experimental results and Monte Carlo simulations for the 5 experimental situations.

Conditions	Polyethylene phantom (ϕ50 mm)				Water phantom (ϕ25 mm)
	Mag. =1.3			Mag. = 2.0	Mag. =1.3
	30 kV	50 kV	80 kV	50 kV	50 kV
Max. Experimental SPR	0.540	0.444	0.452	0.303	0.275
Max. Simulation SPR	0.571	0.472	0.472	0.300	0.289
Diff. @ Max SPR	5.33%	6.03%	4.36%	-0.85%	4.84%
Mean diff. inside phantom	-2.30%	2.35%	1.17%	9.35%	11.19%

The results are summarized in table II where experimental and simulation results of the SPR at the central phantom point are shown together with relative differences between the two approaches at the same central point and as a mean inside the phantom region. It is obvious that higher relative differences are noticed when the global SPR is lower as is the case for a magnification of 2.0 and the water phantom acquisitions.

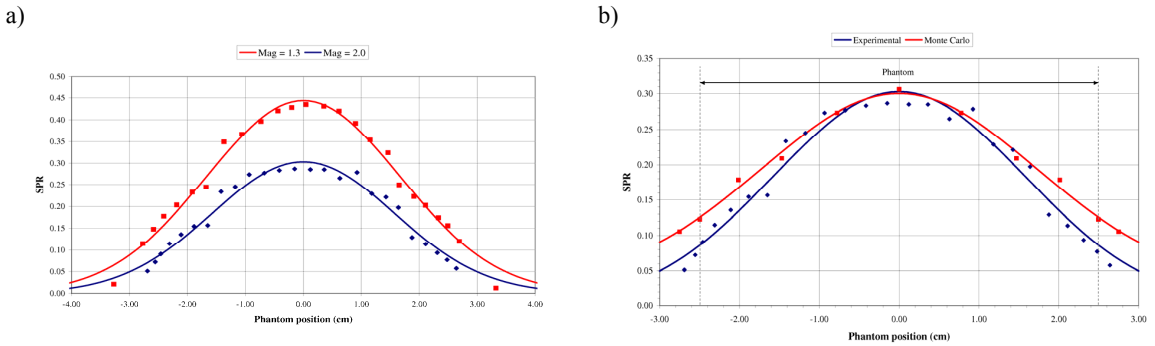

Fig. 4. SPR at different NEMA phantom positions as a function of geometrical magnification at 50 kV. (a) Experimental results for magnifications of 1.3 and 2.0. (b) Comparison between experimental measurements and Monte Carlo simulations for a magnification of 2.0.

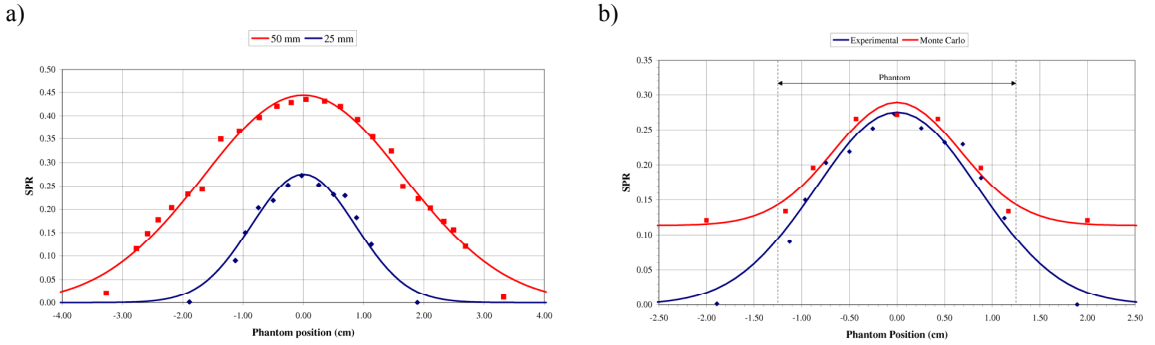

Fig. 5. SPR at different phantom positions as a function of phantom size and composition. (a) Experimental results for NEMA and Water phantom (b) Comparison between experimental and Monte Carlo results with water phantom of 2.5 cm diameter.

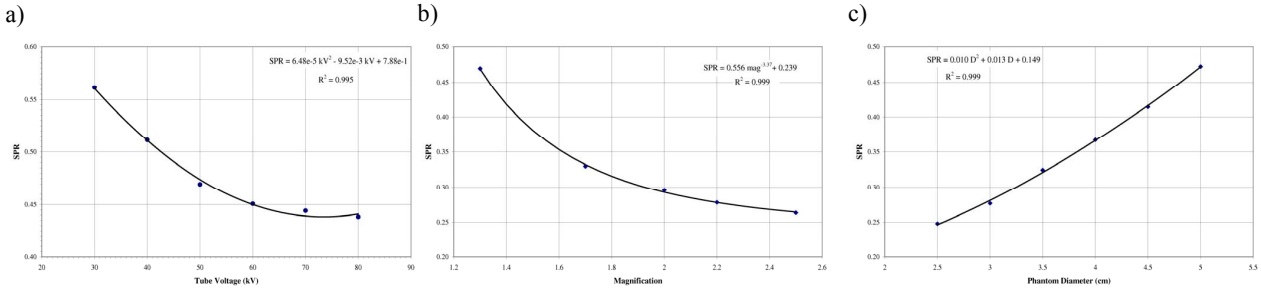

Fig. 6. Interpolation of the maximum SPR assessed using Monte Carlo simulations as a function of: a) tube voltage, b) geometrical magnification, and c) phantom diameter

B. *Influence of acquisition parameters on the SPR*

Following the methodology described by Chen et al.[13], the variation of the maximum SPR value as a function of the various acquisition parameters was assessed using MC simulations. The first test was made by simulating a 50 mm diameter polyethylene phantom with a magnification of 1.3 realized by changing the tube voltage of our simulation from 30 to 80 kV with a step of 10 kV. Fig. 6a shows that the variation of the maximum SPR can be interpolated with a quadratic polynomial function giving a theoretical minimum SPR for a voltage of 73.5 kV (effective energy ~ 40 keV) that can be explained by the competitive effect photon energy-dependent coherent and incoherent scatterings.

The second tested parameter is the magnification which was varied by changing the source to object distance to produce values of 1.3, 1.7, 2.0, 2.2 and 2.5 (Fig. 6b) on a 50 mm diameter polyethylene phantom and tube voltage of 50 kV. Since the scatter should decrease by increasing the distance, the theoretical infinite distance should provide the minimum SPR. For this reason, we have chosen to interpolate the results with a negative power equation which resulted in a minimum asymptotic SPR of 0.239.

Finally we have performed six additional simulations with a magnification of 1.3 and a tube voltage of 50 kV with the polyethylene phantom with a diameter ranging from 2.5 to 5.0 cm (0.5 cm step) to study the influence of the phantom size on the SPR (Fig. 6c). The interpolation curve is again a quadratic polynomial since the scatter increases proportionally to the irradiated volume which is in turn proportional to the square of the phantom diameter.

IV. Discussion

In this paragraph we are going to advance one possible explanation for the high difference between experimental and MC simulation results outside the phantom. To better understand this behaviour, we have performed four additional MC simulations with the polyethylene phantom, a magnification of 1.3 and with a tube potential of 50 kV to track the history of primary and scatter radiation. The diagram of these simulations and one of the standard simulations are shown in Fig. 7 and further explained below:

a) *Before phantom* situation was scored by placing the SSW-SSR cards after the tube filter and *before the phantom*. This will provide an estimation of the primary on and off focal spot corresponding to particles without and with collisions, respectively (*P'* and *P"* for the experimental measurements);

b) *After phantom* situation corresponds to the placement of the SSW-SSR cards just before the detector cover and *after the phantom*, to estimate the scatter produced by the phantom and bed;

c) *After cover* situation is the standard simulation with the SSW-SSR cards placed *after the detector cover* and before the detector to allow the estimation of the increment of scatter produced by the detector cover when the phantom is present;

d) *Background before cover* situation is similar to the *After phantom situation* (b) case but this time the phantom and the bed are not present in the simulation model, thus allowing the estimation of the primary on

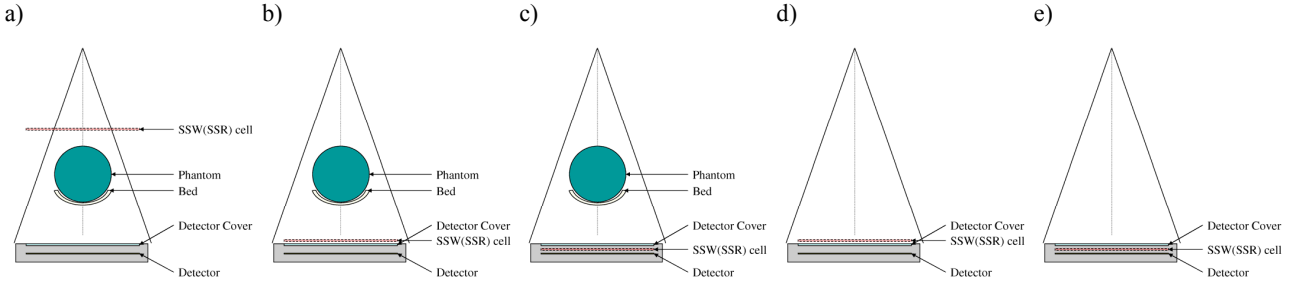

Fig. 7. Illustration of the 5 different MC simulation setups used to illustrate the origins of the difference between experimental and MC results. (a) before phantom, (b) after phantom, c) after cover, d) background before cover, and e) background after cover.

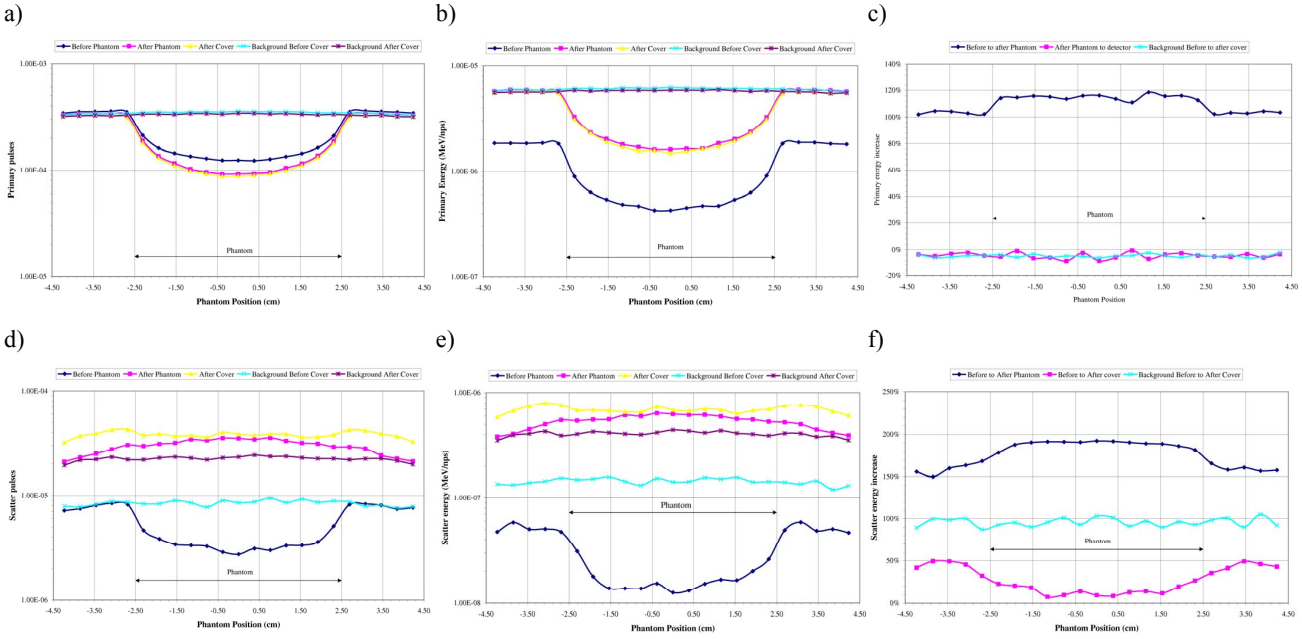

Fig. 8. Primary and scatter evolution at different positions of the micro-CT system. (a) Primary pulses captured by the detector normalized by the number of starting particles. (b) Energy deposited in the detector by the primary. (c) Relative primary energy increase for each step of the simulation. (d) Scatter pulses captured at the detector normalized by the number of starting simulation particles. (e) Energy deposited in the detector by scatter radiation. (f) Relative scatter energy increase for each step of the simulation.

and off focal spot in air (P'_{air} and P''_{air} for the experimental measurements);

e) *Background after cover* situation is a simulation with the SSW-SSR cards located just *after the detector cover* and before the detector, as in the main simulations, but this time without the bed and phantom. This simulation allows the estimation of the scatter produced by the detector cover.

We have to notice that in all previously described situations the results are the obtained at the detector level. It should be also emphasized that in the experimental method equations (1) and (2) correct the intuitive primary measure (M_1) increasing the primary estimate (P') by the addition of scattered radiation mainly from the tube filter (P''), and subtracting this value from the intuitive scatter value (M_2) to obtain the phantom scatter only (S) measurement. On the following example we discuss how this correction can affect the SPR estimation on our micro-CT system mainly because of the presence of the aluminium cover detector.

Fig. 8 shows the primary and scatter evolution through all the previously described steps. It can be seen that the number of primary pulses received by the detector (Fig. 8a) change only in the phantom region. However, the energy deposited on the detector is different because of the phantom presence in the simulation model (Fig. 8b). the increase of the energy between each step (Fig. 8c) shows better that the critical step for the primary seems to be the crossing of the phantom where the change in the primary deposited energy is around 110% while the primary reduction by the detector cover is close to 5%. One possible explanation is that the primary correction that considers all the effects of the imaging device on the primary off focal spot (P'') is important and dependent on the phantom position while this is negligible for the detector cover regardless of the presence of the phantom.

The analysis of the scatter variation, shows that the scatter pulses produced before the phantom (P'') are quite small to arrive at the detector (Figuer 8d), not only because of the distance but also probably because of the detector cover. It can also be seen that the scatter (S) produced on the phantom represents most of the scatter energy arriving to the detector (Figuer 8e). This can be noticed when comparing the scatter energy increase at each step (Fig. 8f) since this increase is about 190% in the phantom region and 150% outside the phantom region. The most important fact is that while the influence of the detector cover on the primary beam is low (5%) and insensitive to the presence of the phantom, this is not the case for the scatter because the cover increases the scatter by ~10% in the phantom region and ~50% outside the phantom region probably because of the high amount of primary arriving to this region that will scatter on the detector cover. One must notice that this amount cannot be estimated experimentally with the correction proposed by Yaffe et al. [26] explaining why we obtain a good agreement between MC simulations and experimental results in the phantom region while in the outer part the scatter is either underestimated by the experimental method and/or overestimated by the MC simulations.

V. Conclusion

We have measured the SPR in the micro-CT subsystem of a commercial preclinical PET-CT scanner and demonstrated that the cone-beam geometry is responsible of its not

negligible magnitude. In this work we also show that the MCNP4C code can be used with confidence to predict the SPR of a micro-CT system also providing an estimation of the contribution of the different components producing the scattered radiation. In this particular device, the detector cover was responsible for a relatively high amount of scatter on the regions where primary photons arrive directly on the cover.

The MCNP4C code is capable to reproduce results of various experimental measurement conditions with good confidence inside the phantom region, especially when modelling conditions produce high SPR. However when the SPR is lower, the relative difference increases (11.2% with ϕ25 mm phantom) because of the global SPR reduction since the absolute difference between experimental and MC simulation results is manly constant (~0.02). MC simulations were valuable for the evaluation of the influence on the maximum SPR value of some acquisition parameters and can be used with confidence for the optimization of system design, acquisition and reconstruction protocols for quantitative structural CT and molecular PET imaging through the generation of accurate attenuation maps for attenuation correction of PET data.

ACKNOWLEDGEMENTS

This work was supported by the Swiss National Science Foundation under grant SNSF 31003A-125246.

REFERENCES

[1] K. B. Parnham, S. Chowdhury, J. Li, D. J. Wagenaar, and B. E. Patt, "Second-generation, tri-modality pre-clinical imaging system," in *IEEE Nuclear Science Symposium Conference Record*, 2006, pp. 1802-1805.

[2] H. Zaidi and B. H. Hasegawa, "Determination of the attenuation map in emission tomography.," *J Nucl Med,* vol. 44, pp. 291-315, 2003.

[3] P. L. Chow, F. R. Rannou, and A. F. Chatziioannou, "Attenuation correction for small animal PET tomographs.," *Phys Med Biol,* vol. 50, pp. 1837-1850, 2005.

[4] R. Prasad, M. R. Ay, O. Ratib, and H. Zaidi, "CT-based attenuation correction on the FLEX Triumph™ preclinical PET/CT scanner," in *Nuclear Science Symposium Conference Record (NSS/MIC), 2009 IEEE*, 2009, pp. 3357-3362.

[5] L. R. MacDonald, K. Iwata, B. E. Patt, J. S. Iwanczyk, A. B. Hwang, M. C. Wu, and B. H. Hasegawa, "Evaluation of x-ray detectors for dual-modality CT-SPECT animal imaging," in *Penetrating Radiation Systems and Applications IV*, Seattle, WA, USA, 2002, pp. 91-102.

[6] R. Gupta, M. Grasruck, C. Suess, S. H. Bartling, B. Schmidt, K. Stierstorfer, S. Popescu, T. Brady, and T. Flohr, "Ultra-high resolution flat-panel volume CT: fundamental principles, design architecture, and system characterization," *Eur Radiol,* vol. 16, pp. 1191-205, Jun 2006.

[7] J. H. Siewerdsen and D. A. Jaffray, "Cone-beam computed tomography with a flat-panel imager: magnitude and effects of x-ray scatter," *Med Phys,* vol. 28, pp. 220-31, Feb 2001.

[8] M. Ay and H. Zaidi, "Assessment of errors caused by x-ray scatter and use of contrast medium when using CT-based attenuation correction in PET.," *Eur J Nucl Med Mol Imaging,* vol. 33, pp. 1301-1313, 2006.

[9] J. M. Boone and V. N. Cooper, "Scatter/primary in mammography: Monte Carlo validation.," *Med Phys,* vol. 27, pp. 1818-1831, Aug 2000.

[10] X. Liu, C. C. Shaw, T. Wang, L. Chen, M. C. Altunbas, and S. C. Kappadath, "An Accurate Scatter Measurement and Correction Technique for Cone Beam Breast CT Imaging Using Scanning Sampled Measurement (SSM) Technique," *Proc Soc Photo Opt Instrum Eng,* vol. 6142, pp. 6142341-6142347, Feb 28 2006.

[11] J. S. Maltz, B. Gangadharan, M. Vidal, A. Paidi, S. Bose, B. A. Faddegon, M. Aubin, O. Morin, J. Pouliot, Z. Zheng, M. M. Svatos, and A. R. Bani-Hashemi, "Focused beam-stop array for the measurement of scatter in megavoltage portal and cone beam CT imaging," *Med Phys,* vol. 35, pp. 2452-62, Jun 2008.

[12] A. L. Kwan, J. M. Boone, and N. Shah, "Evaluation of x-ray scatter properties in a dedicated cone-beam breast CT scanner.," *Med Phys,* vol. 32, pp. 2967-2975, Sep 2005.

[13] Y. Chen, B. Liu, J. M. O'Connor, C. S. Didier, and S. J. Glick, "Characterization of scatter in cone-beam CT breast imaging: Comparison of experimental measurements and Monte Carlo simulation.," *Med Phys,* vol. 36, pp. 857-869, 2009.

[14] Y. C. Ni, M. L. Jan, K. W. Chen, Y. D. Cheng, K. S. Chuang, and Y. K. Fu, "Magnitude and effects of X-ray scatter of a cone-beam micro-CT for small animal imaging.," *Nucl Instr Meth A,* vol. 569, pp. 245-249, 2006/12/20 2006.

[15] P. L. V. Chow, N.T; Chatziioannou, A.F., "Estimating the Magnitude of Scatter in Small Animal Cone-Beam CT," *Nuclear Science Symposium Conference Record, 2004 IEEE,* vol. 5, pp. 2752-2754, 2004.

[16] L. Zhu, Y. Xie, J. Wang, and L. Xing, "Scatter correction for cone-beam CT in radiation therapy.," *Med Phys,* vol. 36, pp. 2258-2268, 2009.

[17] R. Ning, X. Tang, and D. Conover, "X-ray scatter correction algorithm for cone beam CT imaging.," *Med Phys,* vol. 31, pp. 1195-1202, May 2004.

[18] M. Ay and H. Zaidi, "Development and validation of MCNP4C-based Monte Carlo simulator for fan- and cone-beam x-ray CT.," *Phys Med Biol,* vol. 50, pp. 4863-4885, 2005.

[19] J. M. Boone and J. A. Seibert, "Monte Carlo simulation of the scattered radiation distribution in diagnostic radiology.," *Med Phys,* vol. 15, pp. 713-720, 1988.

[20] Y. Kyriakou and W. A. Kalender, "X-ray scatter data for flat-panel detector CT.," *Phys Med,* vol. 23, pp. 3-15, Mar 2007.

[21] Y. Kyriakou and W. A. Kalender, "Efficiency of antiscatter grids for flat-detector CT.," *Phys Med Biol,* vol. 52, pp. 6275-6293, 2007.

[22] Y. Kyriakou, M. Meyer, and W. A. Kalender, "Technical note: comparing coherent and incoherent scatter effects for cone-beam CT.," *Phys Med Biol,* vol. 53, pp. N175-185, May 21 2008.

[23] Y. Kyriakou, T. Riedel, and W. A. Kalender, "Combining deterministic and Monte Carlo calculations for fast estimation of scatter intensities in CT.," *Phys Med Biol,* vol. 51, pp. 4567-4586, Sep 21 2006.

[24] H. Zaidi and M. Ay, "Current status and new horizons in Monte Carlo simulation of X-ray CT scanners," *Med Biol Eng Comput,* vol. 45, pp. 809-817, 2007/09/09/ 2007.

[25] M. R. Ay, P. Gafarian, and H. Zaidi, "A hybrid approach for fast simulation of X-ray computed tomography," in *Proc. IEEE Nuclear Science Symposium and Medical Imaging Conference*, 30.10 - 03.11.2007, Honolulu, Hawaii, 2007, pp. 3155-3160.

[26] M. Yaffe, A. Fenster, and H. E. Johns, "Xenon ionization detectors for fan beam computed tomography scanners," *J Comput Assist Tomogr,* vol. 1, pp. 419-28, Oct 1977.

[27] P. C. Johns and M. Yaffe, "Scattered radiation in fan beam imaging systems," *Med Phys,* vol. 9, pp. 231-9, Mar-Apr 1982.

[28] N. Yagi, M. Yamamoto, K. Uesugi, and K. Inoue, "A large-area CMOS imager as an X-ray detector for synchrotron radiation experiments," *J Synchrotron Radiat,* vol. 11, pp. 347-52, Jul 1 2004.